Joule

CellPress

Article

Bubble growth and departure modes on wettable/non-wettable porous foams in alkaline water splitting

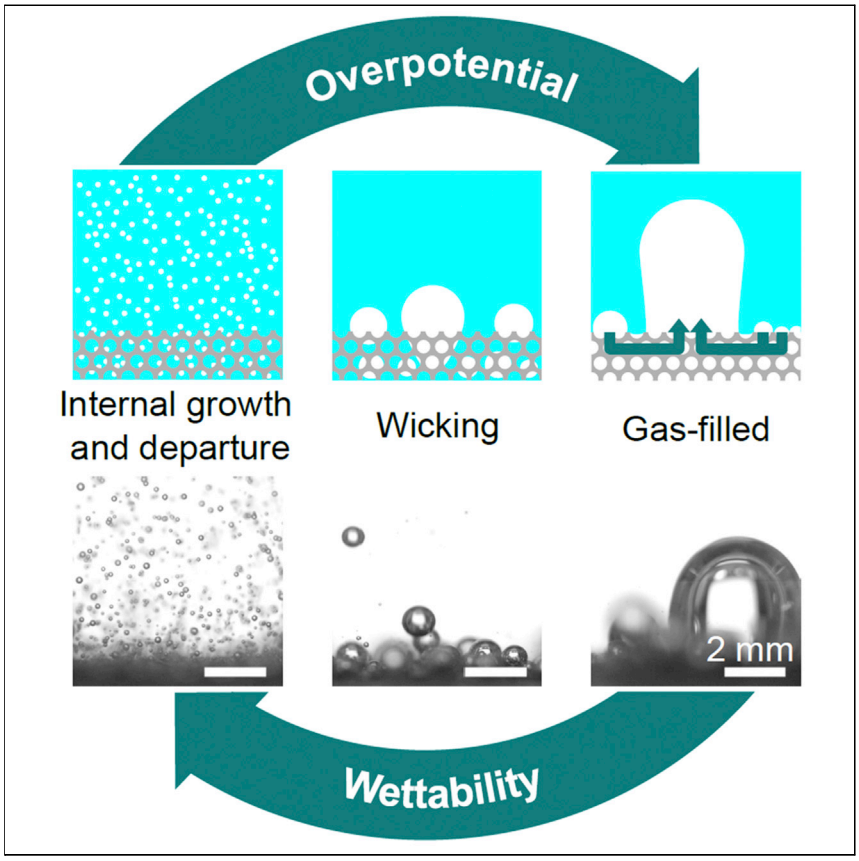

Electrochemical gas-evolving reactions have been widely used for industrial energy conversion and storage processes. Bubbles generated on electrodes create extra transport resistance and induce undesired overpotential. Therefore, the fundamental understanding of bubble dynamics on gas-evolving electrodes is of particular importance. In this work, the relationship among porous electrode wettability, bubble dynamics, and overpotential was investigated. Distinct bubble growth and departure modes for wettable/non-wettable electrodes were observed, leading to a general design guideline for high-performance porous electrodes.

Ryuichi Iwata, Lenan Zhang, Kyle L. Wilke, Shuai Gong, Mingfu He, Betar M. Gallant, Evelyn N. Wang

enwang@mit.edu

HIGHLIGHTS

Drastic transition of bubble dynamics on wettable/non-wettable porous electrodes

Significant change of overpotential on wettable/non-wettable porous electrodes

Design guideline for high-performance porous gas-evolving electrodes

Iwata et al., Joule 5, 887–900
April 21, 2021 © 2021 Elsevier Inc.
https://doi.org/10.1016/j.joule.2021.02.015

Joule

CellPress

Article

Bubble growth and departure modes on wettable/non-wettable porous foams in alkaline water splitting

Ryuichi Iwata,[1,3] Lenan Zhang,[1,3] Kyle L. Wilke,[1] Shuai Gong,[1,2] Mingfu He,[1] Betar M. Gallant,[1] and Evelyn N. Wang[1,4,*]

SUMMARY

Bubble growth and departure are ubiquitous phenomena in gas-evolving reactions, which govern the overall energy and mass transport. However, an in-depth understanding of the relationship between bubble dynamics and the electrochemical processes, in particular, the wettability effect on a gas-evolving porous electrode remains elusive. Here, we report the bubble dynamics and overpotential observed during alkaline water splitting on a polytetrafluoroethylene (PTFE) deposited nickel porous electrode. A slight decrease in hydrophilicity induced a drastic transition of bubble dynamics and a significant increase of the transport overpotential. We show that the porous electrode transitioned from a liquid-filled state to a gas-filled state when varying the wettability, which changed the bubble departure sizes and bubble coverage. As a result, there were substantial changes of the transport overpotential. Our work elucidates the fundamental relationship between wettability and water splitting characteristics, which provides a practical scenario for structuring the electrode for gas-evolving reactions.

INTRODUCTION

Gas-evolving reactions are ubiquitous in many electrochemical systems including water splitting, chlor-alkali electrolysis, and direct methanol fuel cells.[1–8] Bubble formation due to the limited solubility of reactants in the electrolyte reduces the effective reaction area, increases the ohmic resistance, and creates undesired ion concentration, which becomes one of the most dominant mechanisms for overpotential on gas-evolving electrodes.[9–13]

To reduce energy losses and thus improve production efficiency, investigation on gas bubble dynamics in electrochemical systems remains an active topic despite its long history.[1,2,5,14–19] In particular, recent studies showed that the change of wettability of electrodes, enabled by either depositing a hydrophobic material[20] or fabricating micro/nanostructures on a flat substrate,[21–23] plays an important role in bubble dynamics such as heterogeneous nucleation,[24,25] bubble growth,[26,27] and bubble departure size,[20,23] leading to different water splitting characteristics.[23] In a water splitting system, the overpotential is known as the additional voltage required on top of the thermodynamic voltage (1.23 V) to trigger water splitting.[3] During an oxygen evolution reaction process, the total overpotential η_{total} from the reference electrode (RE) to working electrode (WE) consists of the activation overpotential for oxygen evolution reaction (OER) η_{act}, cell ohmic overpotential

Context & scale

Electrochemical gas-evolving reactions play a crucial role in many industrial energy conversion and storage processes. The continuous gas production leads to the evolution of bubbles at the reaction sites, which further result in energy loss due to the increase of transport resistance. To enable high-performance electrochemical systems, bubble dynamics during gas-evolving reactions have attracted particular interest recently. Yet the fundamental relationship among gas-evolving electrode wettability, bubble dynamics, and overpotential has not been well understood. In this work, we investigate the bubble dynamics and the resulting overpotential in alkaline water splitting by engineering the wettability of a porous electrode. The insights gained from this study not only shed light on the fundamentals among electrode wettability, bubble dynamics, and overpotential but also provide design guidelines for porous electrodes to enable high-performance gas-evolving reactions.

$\eta_{ohm,cell}$, bubble ohmic overpotential $\eta_{ohm,bub}$, concentration overpotential η_{con}, and bubble overpotential η_{bub}:

$$\eta_{total} = \eta_{act} + \eta_{ohm,cell} + \eta_{ohm,bub} + \eta_{con} + \eta_{bub} \quad \text{(Equation 1)}$$

Note that the cell ohmic overpotential $\eta_{ohm,cell}$ represents the intrinsic cell ohmic drop due to the circuit and solution resistance, whereas the bubble ohmic overpotential $\eta_{ohm,bub}$ is induced by the bubble layer on the electrode surface.[28,29] The concentration overpotential η_{con} is dominated by the bubble growth-and-departure-induced micro-convection,[30,31] and the bubble overpotential η_{bub} results from the decrease of effective reaction area due to bubble coverage.[10,32,33] Therefore, $\eta_{ohm,bub} + \eta_{con} + \eta_{bub}$ is defined as the transport overpotential η_{trans}, which is closely related to the bubble dynamics on both the anode and cathode and becomes significant for high current density conditions.[3,9,32] At the fundamental level, although engineered flat substrates have been used to study bubble dynamics, the wettability effect on a porous electrode, which is more commonly used in practice due to its high specific area and mass transport performance,[34–40] remains not well understood. Recently, Kempler et al. observed that the bubble dynamics on a micropillar structured electrode vary with the micropillar pitch and diameter, indicating that the wettability of microstructured electrode could play a significant role to bubble behavior.[29] Kang et al. also reported the wettability effect on overpotential using different porous transport layers.[41] However, quantitatively relating the bubble wetting state to bubble dynamics during gas-evolving reactions remains elusive. From a practical perspective, optimizing the electrode porous structure with known material wettability or engineering the wettability based on a fixed porous structure is important for the design of gas-related electrochemical systems. For example, since the kinetics of a given catalyst can be optimized by engineering its wettability,[42,43] it is necessary to fill the knowledge gap and determine how to design the architecture of the porous electrode based on the wettability of the catalyst. This understanding would, therefore, helps bridge fundamental materials insights with practical electrolyzer design.

In this work, we studied the relationship among the porous electrode wettability, bubble dynamics, and the resulting transport overpotential using alkaline water splitting as an example. We measured the transport overpotential on a nickel foam, where its wettability was well controlled through a nickel/polytetrafluoroethylene (PTFE) co-deposition process.[44] By changing the wettability of the electrode with different PTFE coverage Θ_{PTFE} (the ratio of projected PTFE surface area to the total projected area), we show a significant change of the transport overpotential on the same porous structure, which is comparable to or even greater than the activation overpotential for state-of-the-art catalysts at a high current density.[45,46] To understand this phenomenon, we studied the wetting state of the nickel foam with different PTFE coverage (Θ_{PTFE} = 0, 0.16, 0.55, and 0.76). The wetting state transitioned from a superhydrophilic to superhydrophobic state due to the porous structure and PTFE coating, which can be well described by modified Cassie-Baxter and Wenzel equations. The significant change of wetting state led to different bubble growth and departure modes. As a result of the increase in the bubble departure diameter, bubble layer thickness and bubble coverage increased, which contributed to the significant increase in transport overpotential. Based on the insights gained from bubble dynamics, we extracted an important design parameter relating the wettability effect to electrode structure, i.e., the ratio of bubble departure diameter and pore diameter. When the electrode operates in a mass transport loss dominated regime, this ratio should be less than one to ensure that the reaction area enhancement using a porous structure can be maintained.

[1]Department of Mechanical Engineering, Massachusetts Institute of Technology, 77 Massachusetts Avenue, Cambridge, MA 02139, USA

[2]School of Mechanical Engineering, Shanghai Jiao Tong University, 800 Dongchuan Road, Shanghai 200240, China

[3]These authors contributed equally

[4]Lead contact

*Correspondence: enwang@mit.edu

https://doi.org/10.1016/j.joule.2021.02.015

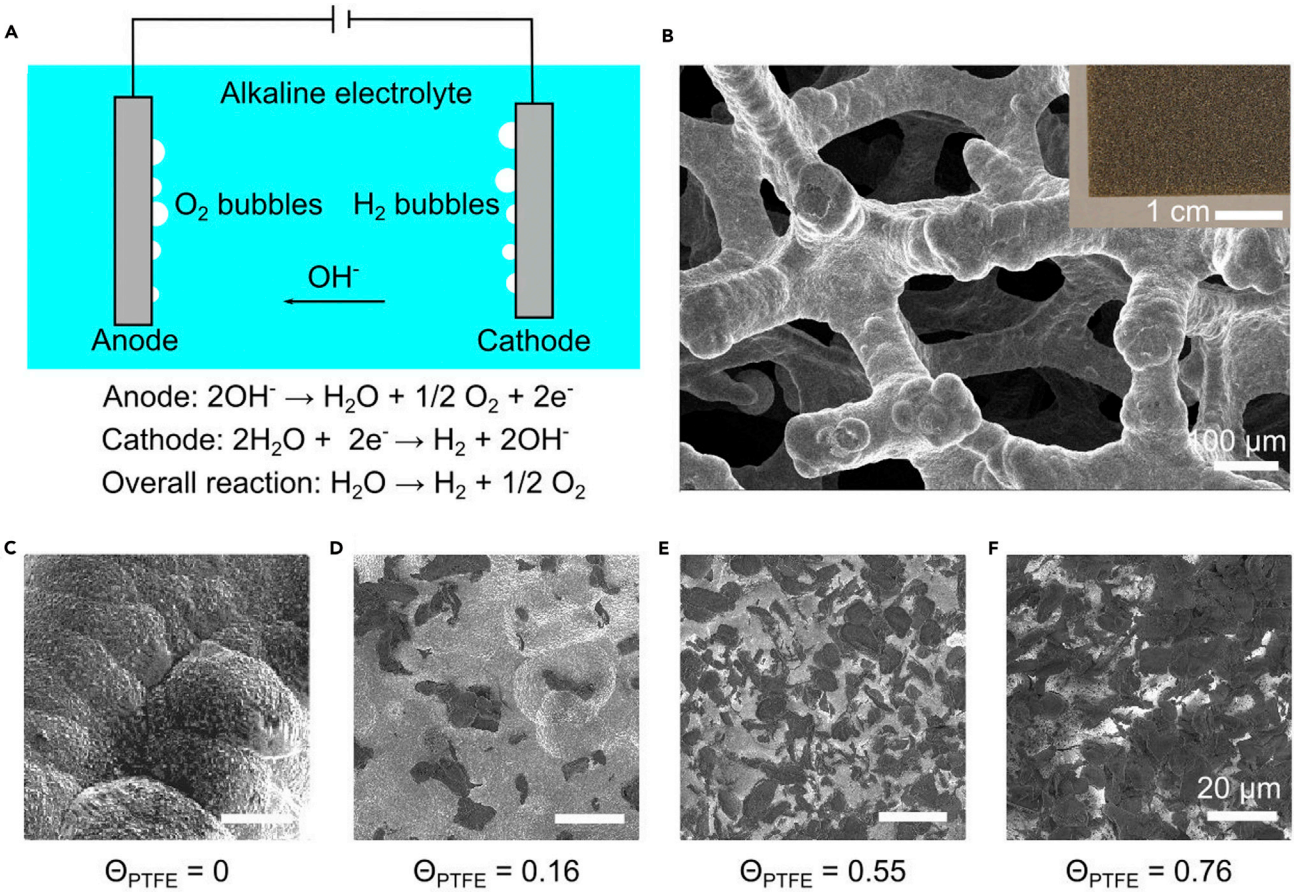

Figure 1. Nickel porous electrodes for water splitting

(A) Schematic of the alkaline water splitting involving an OER and a hydrogen evolution reaction (HER).

(B) SEM image of bare nickel foam (porosity: 95%, number of pores: 20 per 1 cm, thickness: 1.6 mm). The inset image shows the bulk material of the nickel foam.

(C–F) SEM images of nickel foams after electrodeposition. PTFE concentration in the deposition solution are 0, 10, 30, and 45 g/L with deposition time 10, 10, 60, and 45 min, respectively. PTFE coverages were determined based on the SEM images as (C) 0, (D) 0.16 ± 0.02, (E) 0.55 ± 0.03, and (F) 0.76 ± 0.02. Scale bars, all 20 μm.

RESULTS AND DISCUSSION

We studied alkaline water splitting driven by an external electrical potential where oxygen bubbles formed on the anode and hydrogen bubbles formed on the cathode (Figure 1A). Nickel foam with ≈ 95% porosity, ≈ 400 μm pore diameter, and ≈ 1.6 cm thickness was used as the WE for OER. The high porosity and small pore size were confirmed by a scanning electron microscope (SEM, Zeiss Merlin high-resolution SEM) as shown in Figure 1B. In addition, many microscale hierarchical bumpy structures were observed (Figure 1C) on the nickel porous structure, which increased the effective reacting area and the wettability due to the bubbles residing in the Wenzel state.[47] PTFE powders (Goodfellow, ≈ 6–9 μm diameter) were deposited onto the nickel porous structure (Figures 1D–1F). Four nickel foams with various PTFE coverage (0, 0.16 ± 0.02, 0.55 ± 0.03, and 0.76 ± 0.02, respectively) were prepared by changing the concentration of deposition solution and deposition time (see supplemental experimental procedures and Figure S1 for details of sample preparation and PTFE coverage characterization), where the coverage was characterized by SEM (Figures 1C–1F). The reason that the nickel foam coated with PTFE powders was selected as our material system is to achieve a large range of

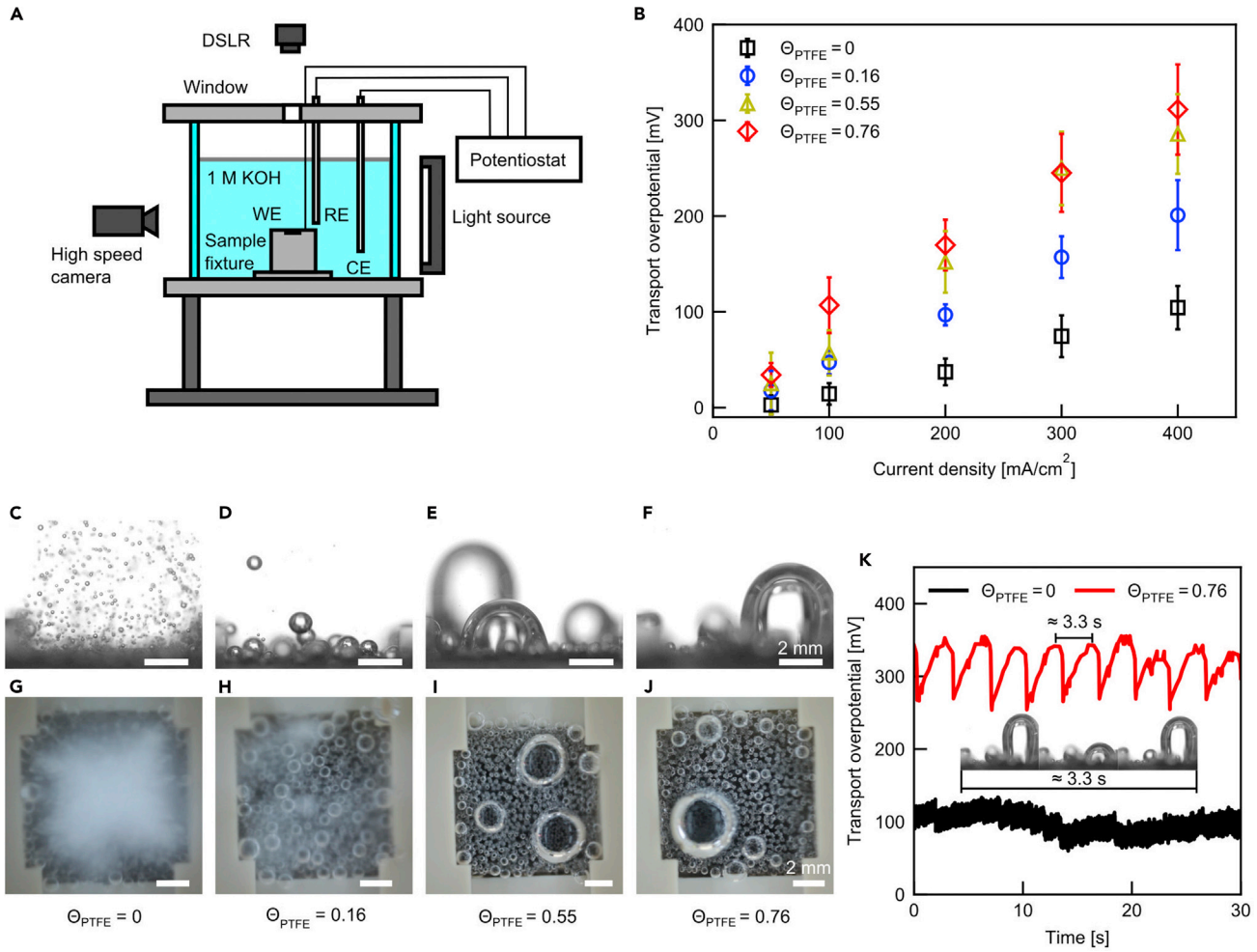

Figure 2. Alkaline water splitting experiments with porous electrodes with various PTFE coverage

(A) Schematic of the water splitting experiment setup. The overpotential at the WE was recorded by a potentiostat. Bubbles were visualized by a high-speed camera from the side and the DSLR from the top.

(B) Transport overpotential as a function of current density. The activation and ohmic overpotentials have been subtracted from the measured overpotential. The error bars represent the standard deviation due to the time average of data points.

(C–F) Side views of oxygen bubbles at 400 mA/cm^2 with PTFE coverage of (C) 0, (D) 0.16, (E) 0.55, and (F) 0.76. Scale bars, all 2 mm.

(G–J) Top views of oxygen bubbles at 400 mA/cm^2 with PTFE coverage of (G) 0, (H) 0.16, (I) 0.55, and (J) 0.76. Scale bars are all 2 mm. The blurriness of images in (G and H) was due to the interference of bubbles.

(K) Time transition of transport overpotentials at 400 mA/cm^2 with PTFE coverage of 0, 0.76. Inset shows the images of repetitive bubble growth on the hydrophobic porous electrode in the interval of 3.3 s, which corresponds to the fluctuation of the transport overpotential.

wettability. This large tunability of wetting state, from superhydrophilic to superhydrophobic, which will be confirmed later, ensures that our analysis can span most of the design conditions for the practical systems.

Figure 2A shows a schematic of a standard three-electrode experimental setup used for our testing (see Figure S2 for details of experimental setup). The nickel foam (10 mm × 10 mm) was horizontally positioned on a sample fixture and used as the WE. The graphite electrode and the Ag/AgCl electrode were used as a counter electrode (CE) and a RE, respectively. The OER polarization curves were obtained by linear sweep voltammetry at a scan rate 1 mV/s. The measured potential was calibrated to the reversible hydrogen electrode (RHE) by the equation: $E_{RHE} = E_{Ag/AgCl} + 0.197\ V + 0.059\ pH$ where E_{RHE} is the potential against RHE and $E_{Ag/AgCl}$ is

the potential against the Ag/AgCl electrode. In addition, OER experiments under constant current density conditions (50, 100, 200, 300, and 400 mA/cm^2) were conducted for bubble visualization and transport overpotential analysis on samples with different PTFE coverage (0, 0.16, 0.55, and 0.76, respectively). To visualize the oxygen bubble dynamics, a high-speed camera (Phantom v7.1, Vision Research Inc.) was placed on the side, and a digital single-lens reflex (DSLR) camera (EOS rebel T3, Canon) was mounted on top, and they were illuminated by a diffuse light source (Fiber-Lite MODEL3100, Dolan-Jenner Industries). The transport overpotential η_{trans} was obtained by subtracting the contribution of the cell ohmic overpotential $\eta_{ohm,cell}$ and activation overpotential η_{act}, which were determined by electrochemical impedance spectroscopy (EIS) and Tafel fitting without the presence of bubbles, respectively (see Figures S3 and S4). The OER process was performed in 1 M KOH solution. Figure 2B shows the transport overpotential as a function of current density with four different PTFE coverages. To investigate the role of wettability and bubble dynamics on the transport overpotential, the overpotential owing to the decrease of effective reaction area with PTFE coverage was carefully calibrated and excluded from the transport overpotential in Figure 2B (see Figure S3). Significant differences in transport overpotential on the WE were obtained by changing PTFE coverage for the wide range of current densities. Specifically, the lowest transport overpotential was observed on the WE without PTFE, whereas it increased over three times when the PTFE coverage increased from 0 to 0.76. As an example, the transport overpotential increased from 104 to 311 mV at a current density of 400 mA/cm^2 when increasing the PTFE coverage from 0 to 0.76. Note that the difference in transport overpotential for non-wettable and wettable electrodes in this experiment was comparable to or even greater than the activation overpotential for state-of-the-art catalysts at a high current density.[45,46] In other words, designing the pore structures and the wettability could be equally important as designing the catalyst to a practical electrolyzer. Meanwhile, a drastic change in the bubble behaviors was observed with the increase of PTFE coverage (Figures 2C–2J), indicating a strong dependence between bubble dynamics and transport overpotential. When no PTFE was deposited on the WE (Θ_{PTFE} = 0), many oxygen bubbles smaller than the pore diameter of the WE (~ 200–700 μm) were generated (Figures 2C and 2G; see Video S1 for bubble dynamics visualization). For PTFE coverage Θ_{PTFE} = 0.16, the oxygen bubbles became much larger than those in the Θ_{PTFE} = 0 condition, which are comparable to the pore diameter (Figures 2D and 2H; see Video S2 for bubble dynamics visualization). A significant transition in bubble behavior was observed when the PTFE coverage increased to Θ_{PTFE} = 0.55, where several very large bubbles (> 2 mm diameter) were observed, while the surrounding bubbles were generally small (< 1 mm diameter, Figures 2E and 2I). Bubbles residing on the WE became the hemispherical shape (Figures 2E and 2I). When the PTFE coverage increased to 0.76, the bubbles behaved similarly to the condition of PTFE coverage Θ_{PTFE} = 0.55, with a slight increase of bubble departure size (≈ 4.5 mm) and transport overpotential. More interestingly, it can be seen that only these large bubbles periodically grew and departed from the WE, whereas most of the surrounding small bubbles remained a residing state for Θ_{PTFE} = 0.55 and 0.76 (see Figure S5; Videos S3 and S4 for bubble dynamics visualization). In addition, a few of the surrounding bubbles could even shrink associated with the simultaneous growth of the neighboring large bubble (see Video S5 for bubble dynamics visualization). Figure 2K shows the time evolution of the transport overpotential for the PTFE coverage of zero and 0.76 under 400 mA/cm^2. Compared with the condition of Θ_{PTFE} = 0, the fluctuation of the transport overpotential for Θ_{PTFE} = 0.76 showed higher amplitude but lower frequency. The frequency of transport overpotential for Θ_{PTFE} = 0.76 was consistent with the departure frequency of the large bubbles (see the inset of Figure 2K; Video S3), indicating the

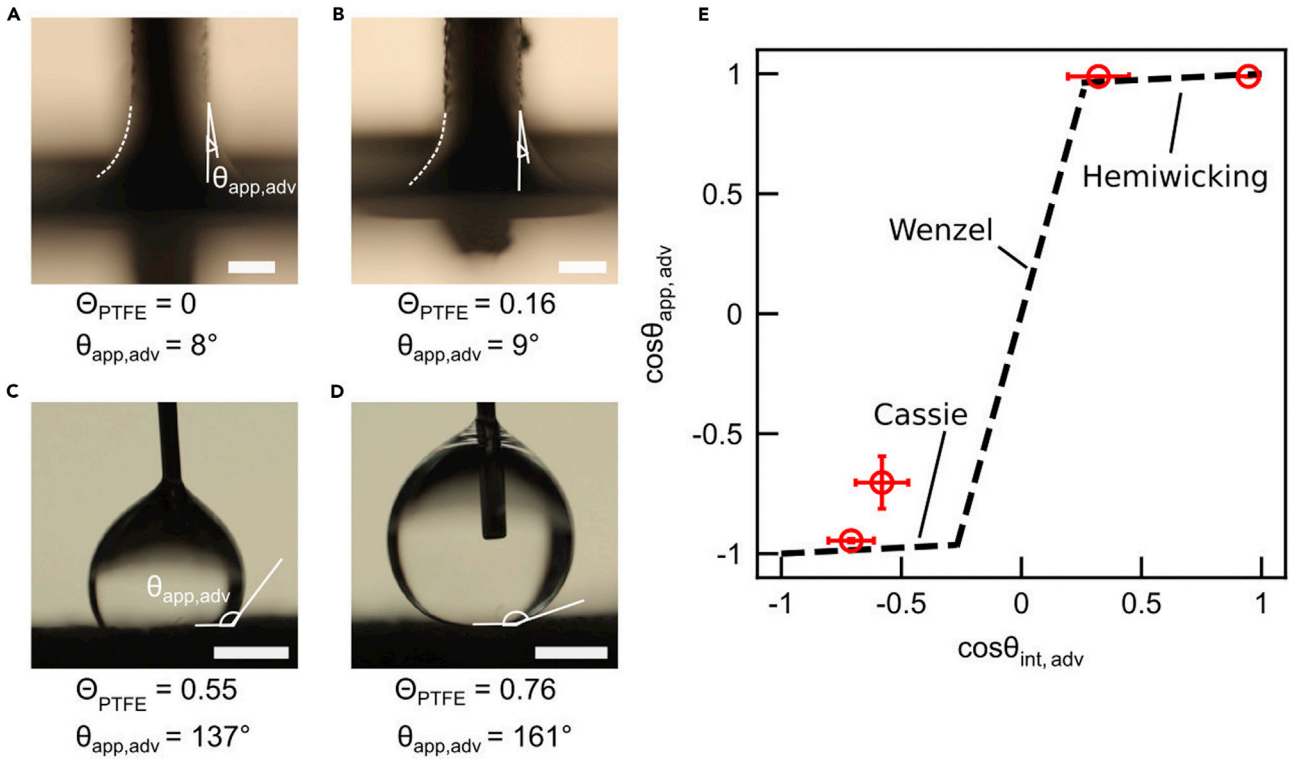

Figure 3. Wettability characterization for wicking/non-wicking porous electrodes with various PTFE coverage

The working fluid is a 1 M KOH solution.

(A and B) Wilhelmy plate method for wicking electrodes. Apparent advancing contact angle $\theta_{app,adv}$ of (A) 8° and (B) 9° with a PTFE coverage Θ_{PTFE} of 0 and 0.16, respectively. Dashed lines represent liquid-gas interfaces. Scale bars, 1 mm.

(C and D) Sessile droplet contact angle measurement for non-wicking electrodes. Apparent advancing contact angle $\theta_{app,adv}$ of (C) 137° and (D) 161° with a PTFE coverage Θ_{PTFE} of 0.55 and 0.76, respectively. Scale bars are 1 mm.

(E) Wetting states of 1 M KOH solution on porous electrodes. The internal advancing contact angle $\theta_{int,adv}$ was estimated from the PTFE coverage. Dashed lines are theoretical predictions for the hemiwicking, Wenzel and Cassie states. The error bars represent the uncertainty for the apparent contact angle measurements and for the internal contact angle estimation.

behavior of these large bubbles plays a significant role in the transport overpotential.[48] To further understand the relationship between the above bubble behaviors and the corresponding transport overpotentials, we characterized the bubble dynamics by leveraging the wetting state analysis as follows of our study.

Figure 3 shows the wettability analysis of WE with different PTFE coverage using 1 M KOH solution. The WE was highly wicking when the PTFE coverage was zero and 0.16 as shown in Figures 3A and 3B. The apparent contact angle was 8° and 9° for the PTFE coverage of zero and 0.16, respectively, which was determined by the Wilhelmy plate method.[49] However, the WE became hydrophobic when the PTFE coverage increased to 0.55 and changed to superhydrophobic (apparent contact angle >150°) when the PTFE coverage further increased to 0.76 as shown in Figures 3C and 3D. We determined the droplet apparent contact angle on the non-wicking WE. A partial Cassie state droplet[50] (137° apparent contact angle) was observed on the WE with the PTFE coverage of 0.55, while a Cassie state droplet (161° apparent contact angle) was seen when the PTFE coverage was 0.76. This significant transition in wetting state can be explained by a combined effect of the porous structure and the PTFE deposition. To quantify this transition behavior, we derived the modified Cassie-Baxter and Wenzel equations, which describe the apparent contact angles of liquid on a composite interface of gas, liquid, and solid material (see

supplemental information for details of wetting state equations). Figure 3E shows that the relationship between the apparent advancing contact angle $\theta_{app,adv}$ and internal contact angle $\theta_{int,adv}$ in all of these four wetting states can be well described by the modified Cassie-Baxter and Wenzel equations (dashed line in Figure 3E), using the experimentally determined solid fraction 0.05 and roughness factor 3.6 as the inputs (see supplemental information for details). Note that the internal contact angle at the inner wall of the porous structure where the surface was chemically heterogenous and rough was determined by placing the droplet on a flat nickel substrate with the same PTFE coverage (see Figure S6 for details).

We explained the significant change in bubble dynamics and transport overpotential considering the wettability effect. In general, the bubble dynamics showed three distinct modes, i.e., internal growth and departure (Figure 4A), wicking (Figure 4B), and gas-filled modes (Figure 4C) due to different bubble growth, departure, and coverage mechanisms. Specifically, in the internal growth and departure mode (Figure 4A), i.e., the WE was not covered by PTFE, bubble nucleation and departure occurred both on the surface and inside of the porous foam because the bubble departure diameter was smaller than the pore diameter (~ 200–700 μm) in this highly wicking state. The bubble departure diameter was 150 $\pm$ 40 μm from a direct measurement of 100 bubbles. We estimated the bubble growth using a combined experiment and modeling approach under the diffuse-controlled growth condition, where an empirical parameter, i.e., the gas efficiency f_g, which is the ratio of the number of molecules used for bubble generation to the total number of molecules generated by the reaction, was incorporated (see supplemental information for details about the bubble growth analysis).[11,51,52] Figure 4D shows the bubble radius R as a function of growth time t for the internal growth and departure mode under 400 mA/cm^2 with different gas efficiencies. The values of f_g were determined from a typical range of gas efficiency which was reported by literature.[51,53] According to this bubble growth analysis, the growth coefficient b (i.e., $R = b\sqrt{t}$) for the internal growth and departure mode ranged from 0.12 to 0.20 mm/s$^{0.5}$ (Table S1).

When the WE was operated in the wicking mode, i.e., the PTFE coverage increased to 0.16, the bubble departure diameter became comparable to the pore diameter due to the slight decrease of wettability. The bubble departure diameter was 450 $\pm$ 390 μm from a direct measurement of 100 bubbles. Although nucleation still occurred both on the surface and inside the WE, direct bubble removal from the internal pores was significantly suppressed because of the increased bubble size and frequent bubble coalescence (Figure 4B). Figure 4E shows the growth of a representative bubble (marked by the red circle in the insets) in the wicking mode under 400 mA/cm^2. The discontinuity of bubble radius at t = 1.2 s indicates the moment of bubble coalescence (see the insets of Figure 4E at t = 1.1 s before coalescence and t = 1.3 s after the coalescence), which can be commonly seen for the bubbles in the wicking mode (see Figure S7A and supplemental information for details). Before coalescence, the evolution of bubble radius followed the diffuse-controlled growth where the growth coefficient of this bubble was 0.26 mm/s$^{0.5}$ in Figure 4E. We characterized more bubbles as shown in Figure S7A. The growth coefficient for the wicking mode ranged from 0.17 to 0.32 mm/s$^{0.5}$, which is comparable to the growth coefficient estimated in the internal growth and departure mode (Table S1).

When the PTFE coverage increased to 0.55 and 0.76, the WE transitioned to a gas-filled mode (Figure 4C). The existence of this gas-filled mode can be confirmed by the following experimental evidence. Specifically, according to the wetting state analysis (Figure 3E), the WE became hydrophobic or superhydrophobic (Figure 3D)

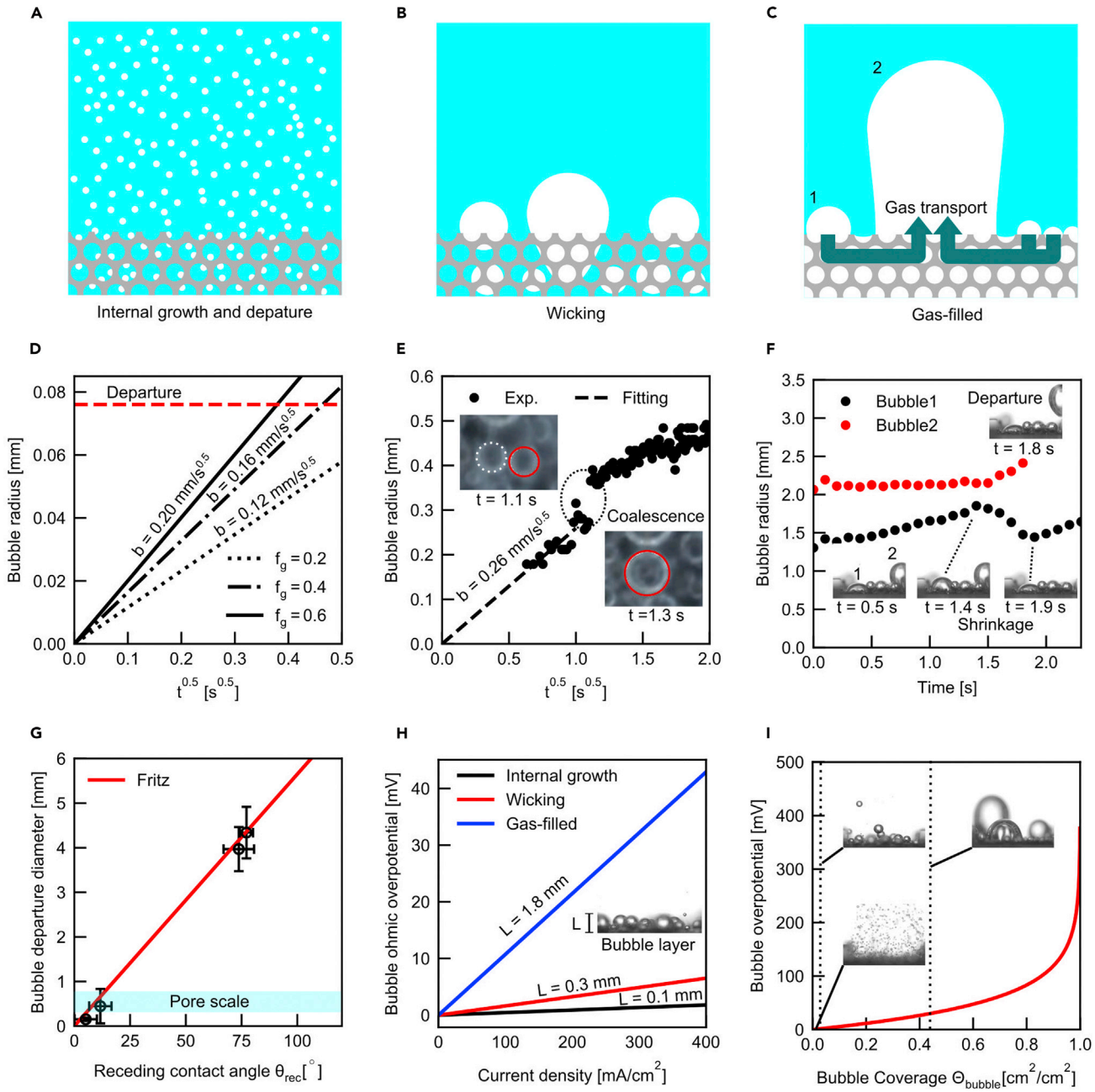

Figure 4. Bubble dynamics on porous electrodes with different wettability and its effect on overpotential

(A–C) Schematics of bubble growth and departure modes.

(A) Hydrophilic electrode and the bubble departure size smaller than the pore size.

(B) Hydrophilic electrode and the bubble departure size comparable to or larger than the pore size.

(C) Hydrophobic electrode where the bubble departure size was dictated by the macroscopic receding contact angle.

(D–F) Characterizations of the bubble growth in the internal growth and departure, wicking, and gas-filled modes.

(D) Bubble radius as a function of time under 400 mA/cm^2 current density in the internal growth and departure mode. The bubble growth was estimated using an experiment and modeling combined approach with the gas efficiency f_g as an empirical parameter (see supplemental information for details).

(E) Bubble radius as a function of time under 400 mA/cm^2 current density in the wicking mode. The discontinuity of bubble radius at 1.2 s is attributed to the bubble coalescence. Insets: top view image before the bubble coalescence (t = 1.1 s) and after the bubble coalescence (t = 1.3 s), where the red circle indicates the bubble being measured and the white dashed circle represent the neighboring bubble interacting with the red circled bubble.

(F) Bubble radius as a function of time under 200 mA/cm^2 current density in the gas-filled mode. Two neighboring bubbles were measured. Insets: time-lapse images of bubble evolution at t = 0.5, 1.4, 1.8, and 1.9 s where the shrinking bubble is marked as bubble 1 and the departed bubble is marked as bubble 2.

Figure 4. *Continued*

(G) Bubble departure diameter as a function of the receding contact angle. The internal receding contact angle and the macroscopic receding contact angle were used for wicking electrodes and non-wicking electrodes, respectively. Solid line shows the Fritz equation. The light blue band indicates the pore diameter (~ 200–700 μm). The error bars are determined from the standard deviations of multiple-time measurements.

(H) Bubble-induced ohmic overpotential as a function of current density for different bubble growth and departure modes. Equation S26 was used for the estimation of bubble-induced ohmic overpotential. The bubble layer thickness and gas void fraction were determined from experimental characterizations (see supplemental information for details). Inset: a side view image of bubbles in the bubble layer.

(I) Bubble overpotential estimation as a function of the bubble coverage. The bubble coverage drastically changes for various bubble departure modes (insets). Equation S8 was used for the estimation. The Tafel slope $RT/\{(1-\alpha)F\} = 0.051$, where α is charge transfer coefficient, F is Faraday constant, R is universal gas constant, and T is temperature, respectively. The dashed lines indicate the experimentally estimated bubble coverages for the internal growth and departure mode, wicking mode, and gas-filled mode, respectively (see supplemental information for details). Insets: side view images for the bubble morphologies in the internal growth and departure, wicking, and gas-filled modes.

and Wenzel bubbles were observed, indicating a strong resistance to liquid filling. Since only the large bubbles could periodically grow and depart from the WE (see Figure S5; Videos S3 and S4), we characterized the growth of these large bubbles under 400 mA/cm^2 (Table S1). Figure S7B shows that the growth coefficient of the large bubbles ranged from 1.4 to 1.6 mm/s$^{0.5}$ which is an order of magnitude larger than the growth coefficients observed in the internal growth and departure and the wick modes under the same current density (400 mA/cm^2). This high growth rate of the large bubbles indicates that there is gas transport from the surrounding small bubbles to the large bubbles through the interconnected pores in the WE, which is driven by the capillary pressure due to the larger curvature of smaller bubbles as sketched in Figure 4C. Therefore, although the radius of large bubbles followed the diffuse-controlled growth relationship, the detailed bubble growth mechanism needs to be further investigated in future work due to the distinct gas transport process in the gas-filled mode. The small bubbles would not grow or depart if the gas generation rate in these bubbles was equal to the gas transport rate from the small bubbles to the large bubbles at a steady state (see Videos S3 and S4). In addition, direct evidence for the gas-filled mode is the shrinking bubble observed in a few of our experiments. Figure 4F shows the evolution of a shrinking bubble (marked by 1 in the inset) and a neighboring growing bubble (marked by 2 in the inset), which can be also seen in Video S5. The bubble 1 slowly grew before 1.4 s followed by a sudden shrinkage between 1.4 and 1.9 s (insets of Figure 4F). Meanwhile, there was simultaneous growth of bubble 2. Bubble 2 departed from the WE at 1.8 s whereas at the same moment, bubble 1 started to grow again. This highly correlated shrinkage and growth shown in bubbles 1 and 2 indicates that these two bubbles were connected through the gaseous pores in the WE.

Figure 4G shows that relationship between the bubble departure diameter and WE wettability can be well captured by the classical Fritz correlation,[54] which equates the bubble holding force at the three-phase contact line with the bubble buoyancy (see Figure S8 for details; $D_b = 0.0208\theta_{app,rec}\{\gamma_{lv}/[g(\rho_l - \rho_v)]\}^{1/2}$ where D_b is the bubble departure diameter, $\theta_{app,rec}$ is the apparent receding contact angle (unit: degree), γ_{lv} is the surface tension, g is the gravitational acceleration, and ρ_l, ρ_g are the density of liquid and gas, respectively). Note that the internal receding contact angle was used for our analysis when the bubble departure diameter was smaller or comparable to the nickel foam pore scale, whereas the apparent receding contact angle was applied when the bubble departure diameter was much larger than the pore scale. The bubble departure diameter for the PTFE coverage of 0.55 and 0.76 was determined from the average of 17 and 28 bubbles, respectively.

The significant change of bubble growth, departure diameter, and wetting state from the internal growth and departure mode to the gas-filled mode leads to the change of bubble coverage, bubble layer thickness, and gas void fraction, which induces

different transport overpotentials. Figure 4H shows the bubble ohmic potential $\eta_{ohm,bub}$ as a function of current density for the internal growth and departure ($\Theta_{PTFE} = 0$), wicking ($\Theta_{PTFE} = 0.16$), and gas-filled ($\Theta_{PTFE} = 0.76$) modes. The bubble ohmic potential $\eta_{ohm,bub}$ was estimated using the experimentally determined bubble layer thickness L and gas void fraction f_b (see supplemental information for details).[28,29] The bubble layer thickness was given by the time average of bubble radius and bubble contact angle, and the void fraction was determined from the time average of bubble volume (see supplemental information for details). Although the gas void fractions were similar for the internal growth and departure mode ($f_b \approx 0.07$), wicking mode ($f_b \approx 0.08$), and gas-filled mode ($f_b \approx 0.08$), the bubble layer thickness L (see the inset of Figure 4H) increased from about 0.1 to 1.8 mm due to the increase of bubble departure diameter, leading to a significant increase of the bubble ohmic overpotential for the gas-filled mode (Figure 4H). On the other hand, Figure 4I shows the bubble overpotential η_{bub} as a function of bubble coverage Θ_{bubble}. In this work, we estimated bubble coverage by analyzing the ratio of total bubble base area to the projected area (10 mm × 10 mm) of the electrode from the top view images and bubble contact angles, which were about 0.001, 0.015, and 0.47 for the internal growth and departure mode ($\Theta_{PTFE} = 0$), wicking mode ($\Theta_{PTFE} = 0.16$), and gas-filled mode ($\Theta_{PTFE} = 0.76$), respectively (see Figure S9 and supplemental information for details). The increase of bubble coverage with PTFE coverage mainly resulted from the increase of bubble contact angle. Note that the experimentally estimated bubble coverage for the projected area (10 mm × 10 mm) is the lower limit of the actual bubble coverage for the entire porous structure, since the bubble covered area inside the porous structure was not taken into account. For the internal growth and departure mode, bubble nucleation and growth should homogeneously occur both inside the porous structure and on the surface of the WE because the bubble departure diameter is smaller than the pore diameter. The experimentally estimated bubble coverage was thus close to the actual bubble coverage in this mode. However, for the gas-filled mode, since the internal porous structure of the WE was covered by gas, the actual bubble coverage can be larger than the experimentally estimated bubble coverage. These experimentally estimated bubble coverages are marked as the dashed lines in Figure 4I, where the induced bubble overpotential can be very small for the internal growth and departure and wicking modes, while it can be comparable with the bubble-induced ohmic overpotential for the gas-filled mode. Compared with the estimated bubble-induced ohmic overpotential and bubble overpotential with the total transport overpotential, the increase of transport overpotential from the internal growth and departure mode to the wicking mode can be attributed to the increase of concentration overpotential. The concentration overpotential could arise from the transport resistance inside the WE, where the species transport inside the porous structure becomes inefficient due to the suppression of bubble removal. Direct experimental characterizations of the concentration overpotential are desirable to further support the above hypothesis, which is practically challenging due to the complex porous nature of the WE. On the other hand, the increase of transport overpotential from the wicking mode to the gas-filled mode mainly resulted from the bubble-induced ohmic overpotential and bubble overpotential, i.e., the transport resistance on the surface of the WE due to the increase of bubble departure diameter and contact angle.

According to the insights gained from the wettability effect and bubble dynamics, we extracted an important design parameter ξ for the porous electrode, i.e., the ratio of the bubble departure diameter to the pore diameter, which triggers the transition from an internal bubble growth and departure mode (Figure 4A) to a wicking mode (Figure 4B). This design parameter indicates that reducing the pore size at the same porosity is not always effective to improve the overall gas production, although more reaction area can be created. A better understanding of bubble de-pinning mechanisms is also

helpful to avoid the transition to the wicking mode.[55] To take full advantage of the surface area enhancement using a porous structure in a mass transport loss dominated regime, the pore size needs to be larger than the bubble departure size on the same electrode to enable efficient bubble removal (i.e., $\xi < 1$), which can be realized by either engineering the pore size without much change of the wettability or tuning the wettability for a fixed pore size in practice. For this reason, a general design procedure can be proposed for the mass transport loss dominated regime. First, for a given wettability, which might be determined from the optimal material kinetics of catalysts, the wetting state of the WE can be predicted by the modified Cassie-Baxter and Wenzel equations. Then, the corresponding bubble departure diameter D_b can be estimated by a correlation such as the Fritz equation with the wetting state as the input. Next, the design parameter ξ can be calculated. If $\xi > 1$, either the pore size or the wettability should be increased. Finally, the above procedures should be iterated with the updated pore size and wettability until $\xi < 1$ is met.

In this work, we demonstrated a significant change in bubble dynamics and transport overpotential during alkaline water splitting observed on the PTFE-deposited nickel foam electrode. We used the nickel foam with various PTFE coverage to change the wetting characteristics from a highly wicking state to superhydrophobic state, which were well predicted by modified Cassie-Baxter and Wenzel equations. The increase of WE hydrophobicity increased the bubble departure diameter, bubble coverage, and bubble layer thickness, and therefore increased the transport overpotential. More importantly, we observed three types of bubble departure and growth modes which are characterized by internal bubble growth and departure, wicking, and gas-filled electrodes. The water splitting performance on porous electrodes is very sensitive to the wettability because the reaction area enhancement due to porous electrode diminishes when the bubble departure size becomes comparable to or larger than the pore size. This result indicates that the ratio of bubble departure diameter and pore diameter is an essential design parameter for high-efficiency water splitting system. The proposed study elucidates the physical insights that relate the wettability effect to the bubble dynamics and overpotential on a porous electrode. Furthermore, when a given catalyst is identified for optimized kinetics at the laboratory scale, this work fills the gaps about how to potentially design the architecture of the electrode based on the wettability of the catalyst and/or substrate and can thus bridge the fundamental materials studies with electrolyzer design.

EXPERIMENTAL PROCEDURES

Resource availability

Lead contact

Further information and requests for resources and materials should be directed to and will be fulfilled by the Lead Contact, Evelyn N. Wang (enwang@mit.edu).

Materials availability

This study did not generate new unique materials.

Data and code availability

Details about the model implementation and the data used in this study can be found in the article and the supplemental information. Requests for further information should be directed to the Lead Contact.

Sample preparation

The nickel porous foam (bulk density 0.45 g/cm^3, thickness 1.6 mm, porosity 95%, Goodfellow) was used as the starting electrode material (Figure 1B). The nickel

porous foam was sonicated in 5 M HCl solution for 20 min to remove oxide layer on the nickel surface (Figure S10). It was subsequently rinsed in deionized (DI) water and ethanol and dried in air flow.

A typical Watt bath was used for the nickel electrodeposition to fabricate the hydrophilic surface. The PTFE powder was added into the Watt bath for the nickel-PTFE co-deposition to obtain the hydrophobic surface.[44] The compositions of chemicals dissolved in DI water are listed in Table S2. The PTFE powder was added in DI water with cetyltrimethylammonium bromide (CTAB) for dispersion. The PTFE dispersion was mixed by a stirrer at 800 rpm for 1 day and sonicated for 60 min. The platinum wire electrode and the Ag/AgCl electrode were used as a CE and a RE, respectively. The nickel porous foam was fixed by an electrode holder and immersed in the electrolyte. The electrolyte was agitated by the stirrer at 400 rpm during the experiment. 1.2 V versus Ag/AgCl of voltage was applied for 10–60 min at 60°C.

Sample characterization

The surface structure of the porous electrodes was visualized by a scanning electron microscopy (Zeiss Merlin high-resolution SEM, Zeiss) with 1.5 kV accelerating voltage. At least, 18 images were taken at different positions for each sample. The average PTFE coverage was estimated from the obtained images.

Alkaline water splitting experiment

All electrochemical experiments with nickel foam were performed on a pool gas-evolving reaction rig shown in Figure 2A. The electrochemical measurements were carried out with a potentiostat (VSP-300, BioLogic). The nickel foam was set on the fixture and connected to the PTFE coated nickel wire (Figure S2). The graphite electrode and the Ag/AgCl electrode were used as a CE and a RE, respectively. Nitrogen gas was induced into the 1 M KOH solution for 15 min to remove dissolved gases before starting experiment. During the experiment, the space above the electrolyte in the bath was filled with nitrogen to prevent dissolution of gases into the electrolyte. The uncompensated resistance between the WE and the RE was measured by EIS (see Figure S4 in supplemental information for details). The overpotential between the WE and the RE for OER in 1 M KOH solution was measured by the linear sweep voltammetry at scan rate 1 mV/s. Current step measurements at 50, 100, 200, 300, and 400 mA/cm^2 were conducted for the bubble visualization and transport overpotential analysis. Oxygen bubbles were visualized by the high-speed camera from the side of the vial. The frame rate and the spatial resolution of the high-speed camera were 100 fps and about 11 μm/pixel, respectively. Moreover, the electrode surface was visualized by the DSLR from the top view. The frame rate and the spatial resolution of the DSLR were 30 fps and about 17 μm/pixel, respectively.

Nickel foam wettability test and analysis

Apparent advancing and receding contact angle on the nickel porous foam was characterized by the Wilhelmy plate method for hydrophilic surfaces and sessile drop method for hydrophobic surfaces. The shape of meniscus on the porous foam was measured with a DSLR (Canon, EOS rebel T3) and a macro lens (MP-E 65 mm f/2.8 x 1–5 Macro Photo, Canon). Contact angles were analyzed by circle and ellipse best fittings with ImageJ. Several measurements, typically five times, were conducted to specify the uncertainty of the measurements. The internal contact angle of nickel foam was estimated from a correlation as a function of PTFE coverage. The correlation was developed based on sessile droplet measurements with PTFE-deposited nickel plates. The specific area of nickel porous foam was

estimated by capillary rise test to estimate the roughness factor (see supplemental information for details).

SUPPLEMENTAL INFORMATION

Supplemental information can be found online at https://doi.org/10.1016/j.joule.2021.02.015.

ACKNOWLEDGMENTS

R.I. acknowledges support from Toyota Central R&D Labs. L.Z. acknowledges support from the Singapore-MIT Alliance for Research and Technology (SMART) LEES Program. K.L.W. acknowledges support from the US-Egypt Science and Technology Joint Fund. This article is derived from the Subject Data funded in part by NAS and USAID, and any opinions, findings, conclusions, or recommendations expressed in this article are those of the authors alone, and do not necessarily reflect the views of USAID or NAS. S.G. acknowledges support from the National Natural Science Foundation of China (grant no. 51706135 and 51521004) and the Shanghai Pujiang Program (grant no. 20PJ1406800). This work was performed in part at MIT MRSEC (Materials Research Science and Engineering Centers) sponsored by the National Science Foundation.

AUTHOR CONTRIBUTIONS

R.I. and L.Z. contributed equally to this work. R.I. and E.N.W. conceived the initial idea and designed experiments. R.I. fabricated the samples and carried out material characterization. R.I., L.Z., K.L.W., S.G., and M.H. performed the experimental analysis. R.I. and L.Z. interpreted the experimental results and performed theoretical analysis. R.I. and L.Z. co-wrote the manuscript with the input from K.L.W., S.G., and M.H.; E.N.W. and B.M.G. edited the manuscript and guided the work.

DECLARATION OF INTERESTS

E.N.W. is a member of the advisory board of *Joule*.

Received: July 7, 2020
Revised: August 20, 2020
Accepted: February 23, 2021
Published: March 19, 2021

REFERENCES

1. Angulo, A., van der Linde, P., Gardeniers, H., Modestino, M., and Fernández Rivas, D. (2020). Influence of bubbles on the energy conversion efficiency of electrochemical reactors. Joule *4*, 555–579.

2. Zhao, X., Ren, H., and Luo, L. (2019). Gas bubbles in electrochemical gas evolution reactions. Langmuir *35*, 5392–5408.

3. Xiang, C., Papadantonakis, K.M., and Lewis, N.S. (2016). Principles and implementations of electrolysis systems for water splitting. Mater. Horiz. *3*, 169–173.

4. Yang, H., Zhao, T.S., and Ye, Q. (2005). In situ visualization study of CO2 gas bubble behavior in DMFC anode flow fields. J. Power Sources *139*, 79–90.

5. Van Der Linde, P., Peñas-López, P., Moreno Soto, Á., Van Der Meer, D., Lohse, D., Gardeniers, H., and Fernández Rivas, D. (2018). Gas bubble evolution on microstructured silicon substrates. Energy Environ. Sci. *11*, 3452–3462.

6. Walter, M.G., Warren, E.L., McKone, J.R., Boettcher, S.W., Mi, Q., Santori, E.A., and Lewis, N.S. (2010). Solar water splitting cells. Chem. Rev. *110*, 6446–6473.

7. Haussener, S., Xiang, C., Spurgeon, J.M., Ardo, S., Lewis, N.S., and Weber, A.Z. (2012). Modeling, simulation, and design criteria for photoelectrochemical water-splitting systems. Energy Environ. Sci. *5*, 9922–9935.

8. Moussallem, I., Jörissen, J., Kunz, U., Pinnow, S., and Turek, T. (2008). Chlor-alkali electrolysis with oxygen depolarized cathodes: history, present status and future prospects. J. Appl. Electrochem. *38*, 1177–1194.

9. Zeng, K., and Zhang, D. (2010). Recent progress in alkaline water electrolysis for hydrogen production and applications. Prog. Energy Combust. Sci. *36*, 307–326.

10. Eigeldinger, J., and Vogt, H. (2000). The bubble coverage of gas-evolving electrodes in a flowing electrolyte. Electrochim. Acta *45*, 4449–4456.

11. Vogt, H., and Balzer, R.J. (2005). The bubble coverage of gas-evolving electrodes in stagnant electrolytes. Electrochim. Acta *50*, 2073–2079.

12. Lee, J.K., and Bazylak, A. (2021). Bubbles: the good, the bad, and the ugly. Joule *5*, 19–21.

13. Lee, J.K., Lee, C., Fahy, K.F., Zhao, B., LaManna, J.M., Baltic, E., Jacobson, D.L., Hussey, D.S., and Bazylak, A. (2020). Critical current density as a performance indicator for gas-evolving

electrochemical devices. Cell Reports Physical Science *1*, 100147.

14. Dukovic, J., and Tobias, C.W. (1987). The influence of attached bubbles on potential drop and current distribution at gas-evolving electrodes. J. Electrochem. Soc. *134*, 331–343.

15. Janssen, L.J.J., Sillen, C.W.M.P., Barendrecht, E., and van Stralen, S.J.D. (1984). Bubble behaviour during oxygen and hydrogen evolution at transparent electrodes in KOH solution. Electrochim. Acta *29*, 633–642.

16. Gabrielli, C., Huet, F., Keddam, M., Macias, A., and Sahar, A. (1989). Potential drops due to an attached bubble on a gas-evolving electrode. J. Appl. Electrochem. *19*, 617–629.

17. Lee, C.H., Zhao, B., Lee, J.K., Fahy, K.F., Krause, K., and Bazylak, A. (2020). Bubble formation in the electrolyte triggers voltage instability in CO2 electrolyzers. iScience *23*, 101094.

18. Lu, Z., Zhang, L., Iwata, R., Wang, E.N., and Grossman, J.C. (2020). Transport-based modeling of bubble nucleation on gas evolving electrodes. Langmuir *36*, 15112–15118.

19. Zhang, L., Iwata, R., Zhao, L., Gong, S., Lu, Z., Xu, Z., Zhong, Y., Zhu, J., Cruz, S., Wilke, K.L., et al. (2020). Nucleation site distribution probed by phase-enhanced environmental scanning electron microscopy. Cell Reports Physical Science *1*, 100262.

20. Brussieux, C., Viers, P., Roustan, H., and Rakib, M. (2011). Controlled electrochemical gas bubble release from electrodes entirely and partially covered with hydrophobic materials. Electrochim. Acta *56*, 7194–7201.

21. Zou, X., Liu, Y., Li, G.D., Wu, Y., Liu, D.P., Li, W., Li, H.W., Wang, D., Zhang, Y., and Zou, X. (2017). Ultrafast formation of amorphous bimetallic hydroxide films on 3D conductive sulfide nanoarrays for large-current-density oxygen evolution electrocatalysis. Adv. Mater. *29*.

22. Fujimura, T., Hikima, W., Fukunaka, Y., and Homma, T. (2019). Analysis of the effect of surface wettability on hydrogen evolution reaction in water electrolysis using micro-patterned electrodes. Electrochem. Commun. *101*, 43–46.

23. Ahn, S.H., Choi, I., Park, H.Y., Hwang, S.J., Yoo, S.J., Cho, E., Kim, H.J., Henkensmeier, D., Nam, S.W., Kim, S.-K., and Jang, J.-H. (2013). Effect of morphology of electrodeposited Ni catalysts on the behavior of bubbles generated during the oxygen evolution reaction in alkaline water electrolysis. Chem. Commun. *49*, 9323–9325.

24. Jones, S.F., Evans, G.M., and Galvin, K.P. (1999). Bubble nucleation from gas cavities - a review. Adv. Colloid Interface Sci. *80*, 27–50.

25. Chen, J., and Guo, L. (2019). Size effect of one-dimensional nanostructures on bubble nucleation in water splitting. Appl. Phys. Lett. *115*.

26. Sakuma, G., Fukunaka, Y., and Matsushima, H. (2014). Nucleation and growth of electrolytic gas bubbles under microgravity. Int. J. Hydr. Energy *39*, 7638–7645.

27. Buehl, W.M., and Westwater, J.W. (1966). Bubble growth by dissolution: influence of contact angle. AIChE J. *12*, 571–576.

28. Leistra, J.A., Sides, P.J., Soc, J.E., Leistra, J.A., and Sides, P.J. (1987). Voltage components at gas evolving electrodes. J. Electrochem. Soc. *134*, 2442–2446.

29. Kempler, P.A., Coridan, R.H., and Lewis, N.S. (2020). Effects of bubbles on the electrochemical behavior of hydrogen-evolving Si microwire arrays oriented against gravity. Energy Environ. Sci. *13*, 1808–1817.

30. Vogt, H. (1990). The concentration overpotential of gas evolving electrodes as a multiple problem of mass transfer. J. Electrochem. Soc. *137*, 1179–1184.

31. Vogt, H., and Stephan, K. (2015). Local microprocesses at gas-evolving electrodes and their influence on mass transfer. Electrochim. Acta *155*, 348–356.

32. Vogt, H. (2013). On the various types of uncontrolled potential increase in electrochemical reactors - the anode effect. Electrochim. Acta *87*, 611–618.

33. Vogt, H. (2017). The quantities affecting the bubble coverage of gas-evolving electrodes. Electrochim. Acta *235*, 495–499.

34. Lu, X., and Zhao, C. (2015). Electrodeposition of hierarchically structured three-dimensional nickel-iron electrodes for efficient oxygen evolution at high current densities. Nat. Commun. *6*, 6616.

35. Liu, J., Wang, J., Zhang, B., Ruan, Y., Lv, L., Ji, X., Xu, K., Miao, L., and Jiang, J. (2017). Hierarchical NiCo2S4@NiFe LDH heterostructures supported on nickel foam for enhanced overall-water-splitting activity. ACS Appl. Mater. Interfaces *9*, 15364–15372.

36. Rao, Y., Wang, Y., Ning, H., Li, P., and Wu, M. (2016). Hydrotalcite-like Ni(OH)2 nanosheets in situ grown on nickel foam for overall water splitting. ACS Appl. Mater. Interfaces *8*, 33601–33607.

37. Zhang, P., Li, L., Nordlund, D., Chen, H., Fan, L., Zhang, B., Sheng, X., Daniel, Q., and Sun, L. (2018). Dendritic core-shell nickel-iron-copper metal/metal oxide electrode for efficient electrocatalytic water oxidation. Nat. Commun. *9*, 381.

38. Jian, J., Yuan, L., Qi, H., Sun, X., Zhang, L., Li, H., Yuan, H., and Feng, S. (2018). Sn−Ni3S2 ultrathin nanosheets as efficient bifunctional water- splitting catalysts with a large current density and low overpotential. ACS Appl. Mater. Interfaces *10*, 40568–40576.

39. You, B., Jiang, N., Sheng, M., Bhushan, M.W., and Sun, Y. (2016). Hierarchically porous urchin-like Ni2P superstructures supported on nickel foam as efficient bifunctional electrocatalysts for overall water splitting. ACS Catal. *6*, 714–721.

40. Chaudhari, N.K., Jin, H., Kim, B., and Lee, K. (2017). Nanostructured materials on 3D nickel foam as electrocatalysts for water splitting. Nanoscale *9*, 12231–12247.

41. Kang, Z., Alia, S.M., Young, J.L., and Bender, G. (2020). Effects of various parameters of different porous transport layers in proton exchange membrane water electrolysis. Electrochim. Acta *354*, 136641.

42. Stoerzinger, K.A., Hong, W.T., Azimi, G., Giordano, L., Lee, Y.L., Crumlin, E.J., Biegalski, M.D., Bluhm, H., Varanasi, K.K., and Shao-Horn, Y. (2015). Reactivity of perovskites with water: role of hydroxylation in wetting and implications for oxygen electrocatalysis. J. Phys. Chem. C *119*, 18504–18512.

43. Wakerley, D., Lamaison, S., Ozanam, F., Menguy, N., Mercier, D., Marcus, P., Fontecave, M., and Mougel, V. (2019). Bio-inspired hydrophobicity promotes CO2 reduction on a Cu surface. Nat. Mater. *18*, 1222–1227.

44. Iacovetta, D., Tam, J., and Erb, U. (2015). Synthesis, structure, and properties of superhydrophobic nickel-PTFE nanocomposite coatings made by electrodeposition. Surface and Coatings Technology *279*, 134–141.

45. McCrory, C.C.L., Jung, S., Peters, J.C., and Jaramillo, T.F. (2013). Benchmarking heterogeneous electrocatalysts for the oxygen evolution reaction. J. Am. Chem. Soc. *135*, 16977–16987.

46. Zou, X., and Zhang, Y. (2015). Noble metal-free hydrogen evolution catalysts for water splitting. Chem. Soc. Rev. *44*, 5148–5180.

47. Wenzel, R.N. (1936). Resistance of solid surfaces to wetting by water. Ind. Eng. Chem. *28*, 988–994.

48. Gabrielli, C., Huet, F., and Nogueira, R.P. (2005). Fluctuations of concentration overpotential generated at gas-evolving electrodes. Electrochim. Acta *50*, 3726–3736.

49. de Gennes, P.-G., Brochard-Wyart, F., and Quéré, D. (2004). Capillarity and Wetting Phenomena (Springer Science & Business Media).

50. Su, J., Charmchi, M., and Sun, H. (2016). A study of drop-microstructured surface interactions during dropwise condensation with quartz crystal Microbalance. Sci. Rep. *6*, 35132.

51. Vogt, H. (1984). The rate of gas evolution of electrodes–I. An estimate of the efficiency of gas evolution from the supersaturation of electrolyte adjacent to a gas-evolving electrode. Electrochim. Acta *29*, 167–173.

52. Van Der Linde, P., Moreno Soto, Á., Peñas-López, P., Rodríguez-Rodríguez, J., Lohse, D., Gardeniers, H., Van Der Meer, D., and Fernández Rivas, D. (2017). Electrolysis-driven and pressure-controlled diffusive growth of successive bubbles on microstructured surfaces. Langmuir *33*, 12873–12886.

53. Chin Kwie Joe, J.M., Janssen, L.J.J., van Strelen, S.J.D., Verbunt, J.H.G., and Sluyter, W.M. (1988). Bubble parameters and efficiency of gas bubble evolution for a chlorine-, a hydrogen- and an oxygen-evolving wire electrode. Electrochim. Acta *33*, 769–779.

54. Fritz, W. (1935). Maximum volume of vapor bubbles. Physik. Zeitschr. *36*, 379–384.

55. Lohse, D., and Zhang, X. (2015). Surface nanobubbles and nanodroplets. Rev. Mod. Phys. *87*, 981–1035.

Joule, Volume *5*

Supplemental information

Bubble growth and departure modes on wettable/non-wettable porous foams in alkaline water splitting

Ryuichi Iwata, Lenan Zhang, Kyle L. Wilke, Shuai Gong, Mingfu He, Betar M. Gallant, and Evelyn N. Wang

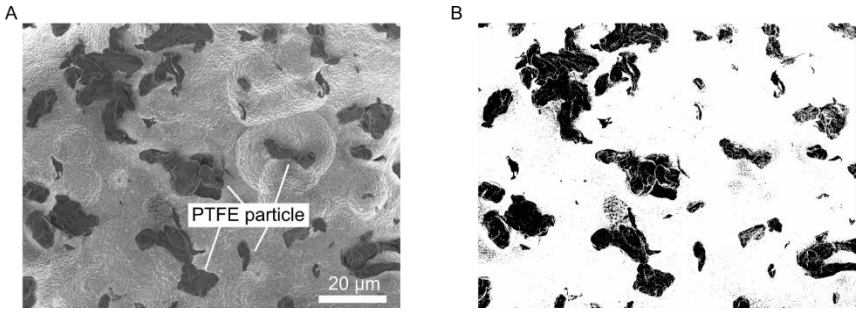

Figure S1. Representative SEM images for PTFE coverage analysis.

(A) The SEM image of PTFE deposited nickel foam. Average PTFE coverage, 0.16. Scale bar, 20 μm.

(B) The binary image of the PTFE deposited nickel foam surface.

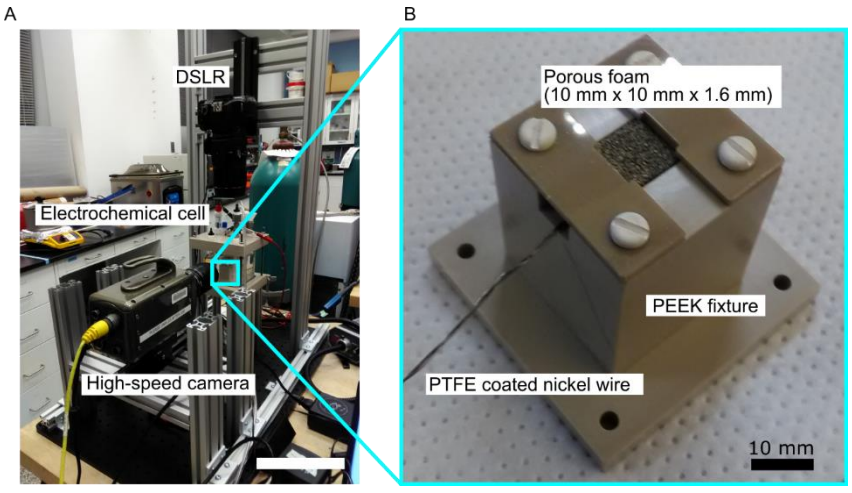

Figure S2. Experimental setup for electrochemical measurements.

(A) Overview of the experimental setup. Scale bar, 20 cm.

(B) Working electrode and its holder and connection. Scale bar, 10 mm.

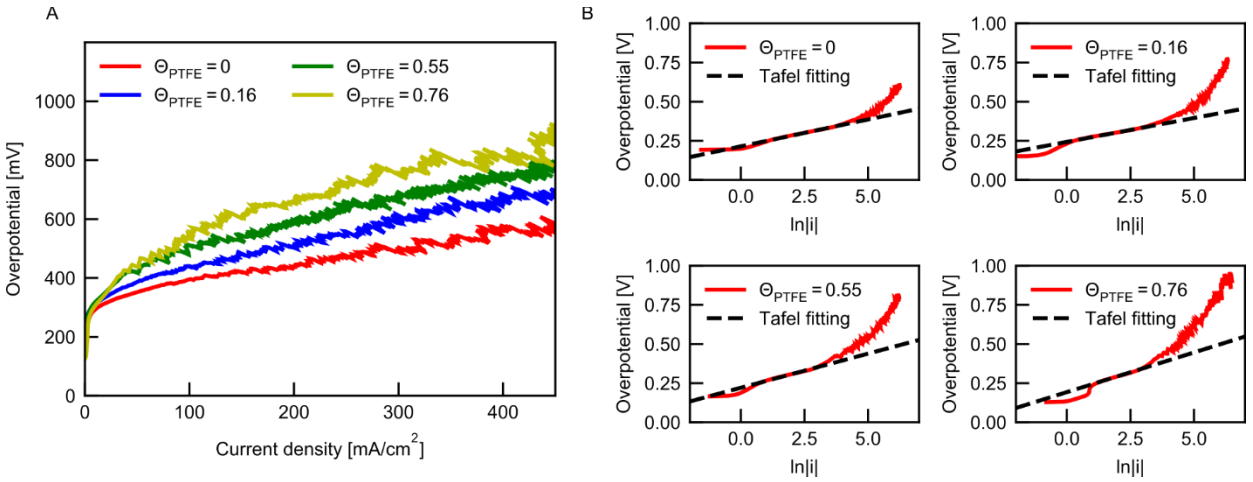

Figure S3. Electrochemical performances for porous electrodes with different PTFE coverages.

(A) OER polarization curves for porous electrodes. The ohmic overpotential has been subtracted from the measured overpotential. The uncompensated resistance is determined by electrochemical impedance spectroscopy. The fluctuation of the curves is associated with bubble detachment.

(B) Tafel plots for porous electrodes. The kinetic parameters for each electrode are determined from these plots. The deviation from the linear fit observed in the low overpotential region (< 0.24 V) is due to the charging current of high surface area electrodes. Thus, the Tafel fitting was only performed in the linear region with overpotential from about 0.24 V to 0.37 V.

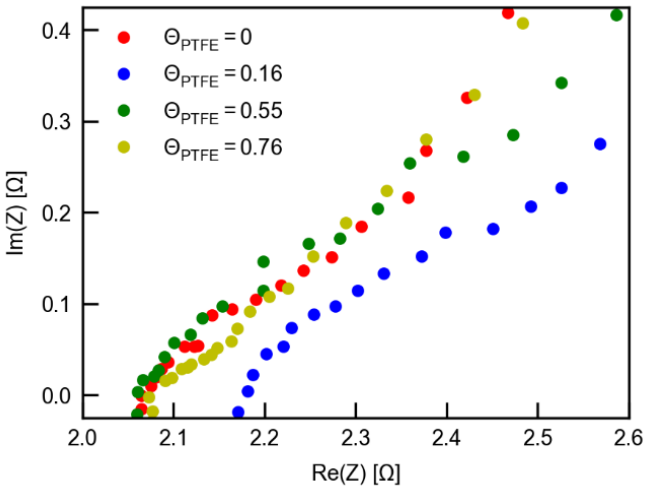

Figure S4. Electrochemical impedance spectroscopy for porous electrodes with various PTFE coverage for frequencies of 200 kHz to 1 Hz at a sampling rate of 6 points/dec. The uncompensated cell resistances for PTFE coverage of 0, 0.16, 0.55, 0.76 are 2.07, 2.18, 2.06, 2.1 Ω, respectively.

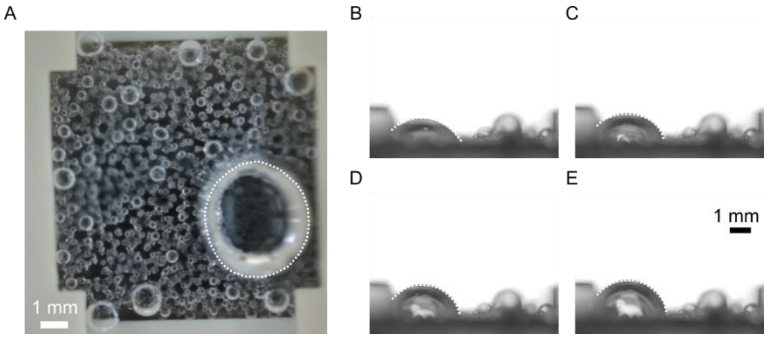

Figure S5. Bubble distribution for the gas-filled mode from the (A) top view and (B), (C), (D) and (E) side view (100 ms/frame) under 400 mA/cm^2 current density, where only the largest bubble marked by the white-dashed line is active.

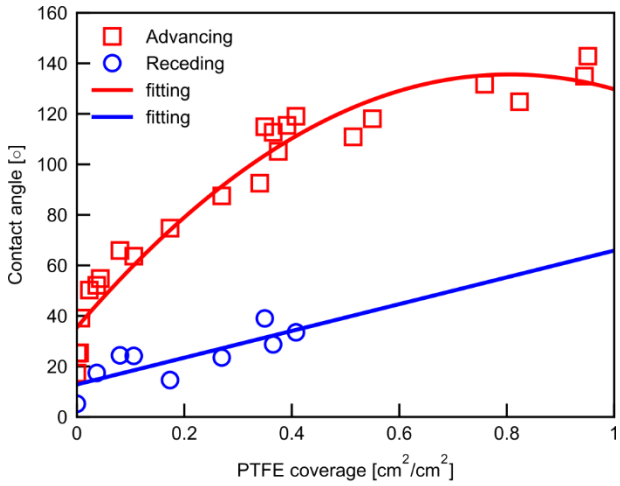

Figure S6. Contact angle measurement of 1 M KOH solution droplets on PTFE deposited nickel plates.

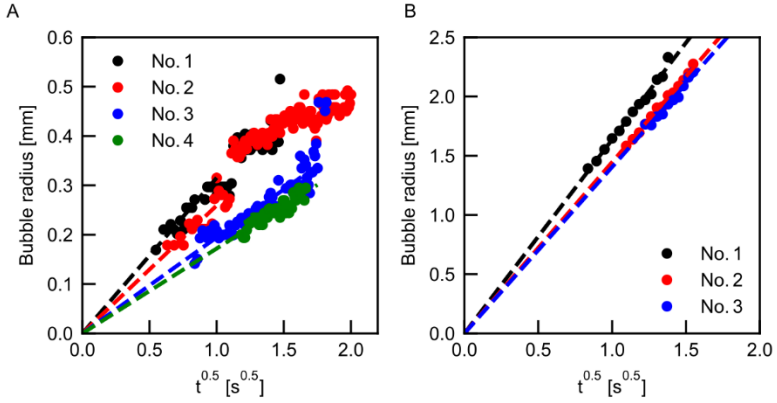

Figure S7. Bubble growth for (A) the wicking mode (Θ_{PTFE} = 0.16) and (B) the gas-filled mode (Θ_{PTFE} = 0.76). The growth rate coefficients in these plots are listed in Table S1.

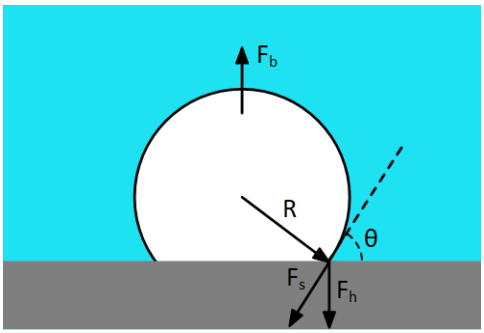

Figure S8. Schematic for the derivation of the Fritz equation, which predicts the bubble departure diameter.

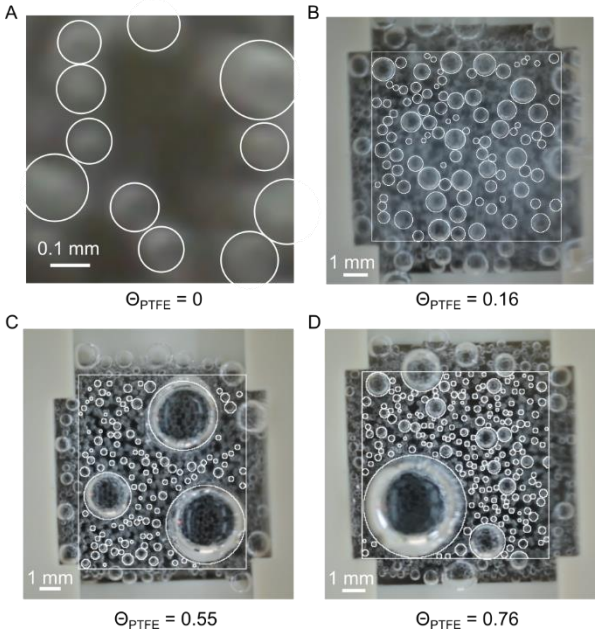

Figure. S9. Bubbles covered porous electrodes with various PTFE coverages ((A) Θ_{PTFE} = 0, (B) Θ_{PTFE} = 0.16, (C) Θ_{PTFE} = 0.55 and (D) Θ_{PTFE} = 0.76). For bubble population and bubble coverage analysis, 97, 99, 124 and 205 bubbles were counted for PTFE coverages Θ_{PTFE} = 0, 0.16, 0.55 and 0.76.

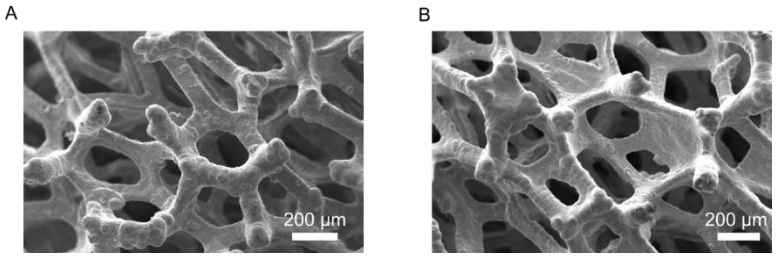

Figure S10. SEM images of the nickel porous foams. (A) Bare porous foam before the treatment. (B) Porous foam after the HCl cleaning and sonication.

Table S1. Bubble growth characterization under 400 mA/cm^2 for the porous electrode with different PTFE coverages

The growth coefficient b was obtained by fitting the bubble radius to the diffuse-controlled growth relationship. Multiple measurements were performed on different bubbles.

Θ_{PTFE}	0	0.16	0.76
Mode	Internal growth *1	Wicking *2	Gas-filled *3
b ($R = b\sqrt{t}$)	0.12 mm/s$^{0.5}$ 0.16 mm/s$^{0.5}$ 0.20 mm/s$^{0.5}$	0.32 mm/s$^{0.5}$ 0.26 mm/s$^{0.5}$ 0.19 mm/s$^{0.5}$ 0.17 mm/s$^{0.5}$	1.64 mm/s$^{0.5}$ 1.45 mm/s$^{0.5}$ 1.4 mm/s$^{0.5}$

*1 Estimated from models assuming the gas efficiency f_g = 0.2, 0.4, 0.6, respectively.

*2 Experimental data for four bubbles.

*3 Experimental data for three bubbles.

Table S2. Chemical composition in electroplating solution.

Component	Amount
Nickel(II) sulfate hexahydrate, $NiSO_4 \cdot 6H_2O$ (Sigma Aldrich)	300 g/L
Nickel(II) Chloride hexahydrate, $NiCl_2 \cdot 6H_2O$ (Sigma Aldrich)	45 g/L
Boric acid, H_3BO_3 (Sigma Aldrich)	45 g/L
PTFE powder (Particle diameter: 6-9 μm, Goodfellow)	0, 3, 30, 45 g/L
Cetyltrimethylammonium bromide, CTAB (Sigma Aldrich)	0.033 g/g$_{PTFE}$

Supplemental Experimental Procedures

Note 1 – Overpotential at anode

For large values of overpotential, the cathodic component of the current is negligible. Therefore, the charge transfer overpotential η_{ct} at the anode is estimated by the simplified current-overpotential equation,

$$\eta_{ct} = \frac{R_g T}{(1-\alpha)F} ln\left(\frac{i}{i_0}\frac{C_{bulk}}{C_s}\right) \quad \text{(Eq. S1)}$$

where α is charge transfer coefficient, F is faraday constant, R_g is universal gas constant, T is temperature, i_0 is exchange current density, C_{bulk} is ion concentration in bulk, and C_s is ion concentration at the electrode surface.

In practice, it is convenient to use the projected area A_{proj} to define the nominal current density,

$$i_{nominal} = \frac{I}{A_{proj}}. \quad \text{(Eq. S2)}$$

where I is the current. This definition is used for the current density in this paper unless otherwise specified.

A roughness factor rf_{ECSA} is defined as the ratio of the electrochemically active surface area (ECSA) A_{ECSA} to the projected area,

$$rf_{ECSA} \equiv \frac{A_{ECSA}}{A_{proj}}. \quad \text{(Eq. S3)}$$

The gas evolving electrode is covered with bubbles which lead to inactive areas on the surface[1,2]. Thus, the actual current density i can be defined as

$$i \equiv \frac{I}{rf_{ECSA}\, A_{proj}(1-\Theta_{bubble})} = \frac{i_{nominal}}{rf_{ECSA}(1-\Theta_{bubble})} \quad \text{(Eq. S4)}$$

where Θ_{bubble} is the bubble coverage. Combining the Eq. S1 and Eq. S4,

$$\eta_{ct} = \frac{R_g T}{(1-\alpha)F}\left\{ln\left(\frac{i_{nominal}}{rf_{ECSA}(1-\Theta_{bubble})i_0}\right) - ln\left(\frac{C_s}{C_{Bulk}}\right)\right\}$$

$$= \frac{R_g T}{(1-\alpha)F} ln\left(\frac{i_{nominal}}{rf_{ECSA} i_0}\right) - \frac{R_g T}{(1-\alpha)F} ln(1-\Theta_{bubble}) - \frac{R_g T}{(1-\alpha)F} ln\left(\frac{C_s}{C_{Bulk}}\right). \quad \text{(Eq. S5)}$$

The first, second and third terms describe the activation overpotential, the bubble overpotential and the concentration overpotential, respectively. The bubble overpotential and the concentration overpotential are consolidated as the transport overpotential. Thus, the charge-transfer overpotential can be described as follows:

$$\eta_{ct} = \eta_{act} + \eta_{bub} + \eta_{con}\,, \quad \text{(Eq. S6)}$$

$$\eta_{act} = \frac{R_g T}{(1-\alpha)F} ln\left(\frac{i_{nominal}}{rf_{ECSA} i_0}\right)$$

$$= \frac{R_g T}{(1-\alpha)F}\{ln(i_{nominal}) - ln(rf_{ECSA} i_0)\}, \quad \text{(Eq. S7)}$$

$$\eta_{bub} + \eta_{con} = \frac{R_g T}{(1-\alpha)F}\left\{-ln(1-\Theta_{bubble}) - ln\left(\frac{C_s}{C_{Bulk}}\right)\right\}. \quad \text{(Eq. S8)}$$

The Eq. S7 is used to estimate the activation overpotential from the Tafel plot assuming the transport overpotential is negligible when the current density is small (Figure S3B).

Note 2 – Wetting state analysis

Here, we analyze wetting state of the heterogeneously PTFE coated nickel foam. The contact angle of a bubble on a porous foam (apparent contact angle) is different from the one on its wall of porous foam (internal contact angle). PTFE particles were heterogeneously deposited on the surface of the nickel foam. The internal contact angle on the wall of nickel foam in Wenzel state can be described as

$$cos\theta_{int} = rf_{local,1}sf_{1,local}cos\theta_1 + rf_{local,2}sf_{2,local}cos\theta_2. \quad \text{(Eq. S9)}$$

rf_{local} is the roughness factor of each component which is defined as the total surface area of each component to the cross-sectional area of each component and $sf_{,\text{local}}$ is the solid fraction of each component on the substrate which is defined as the ratio of the projected surface area of each component to the total cross-sectional surface area. Subscript 1 and 2 denote PTFE and nickel, respectively. We prepared PTFE deposited nickel plates with different PTFE coverages and characterized the contact angles of 1 M KOH solution on these samples (Figure S6). The PTFE coverage is defined as the ratio of the projected area of PTFE to the projected area of the total surface. The PTFE coverage for each sample was characterized based on binarized SEM images as shown in Figure S1. The average PTFE coverage for each sample with the standard error in Figure 1C-F, which was obtained from at least 18 images, were 0, 0.16 ± 0.02, 0.55 ± 0.03 and 0.76 ± 0.02, respectively.

Note 3 – Apparent contact angle on a porous foam

The apparent contact angle of a droplet on a surface of a porous material consists of component 1 and component 2. The third component is a fluid which fills the porous material. Therefore, a modified Cassie-Baxter equation can be described as

$$cos\theta_{app} = rf_{local,1}sf_1 cos\theta_1 + rf_{local,2}sf_2 cos\theta_2 + (1 - sf_1 - sf_2)cos\theta_3, \quad \text{(Eq. S10)}$$

$$sf_{1,local} + sf_{2,local} = 1, \quad \text{(Eq. S11)}$$

$$sf_1 = sf_{1,local}(sf_1 + sf_2), \quad \text{(Eq. S12)}$$

$$sf_2 = sf_{2,local}(sf_1 + sf_2) \quad \text{(Eq. S13)}$$

where θ_{app} is the apparent contact angle, θ_1 and θ_2 are the intrinsic contact angle, and sf is the solid fraction defined as the ratio of the projected surface area of the component to the cross-sectional surface area of the porous foam. For a droplet in a hemiwicking state, $\cos\theta_3 = 1$. Substituting Eq. S9 into Eq. S10,

$$cos\theta_{app} = (1 - sf_1 - sf_2) + (sf_1 + sf_2)cos\theta_{int}. \quad \text{(Eq. S14)}$$

For a droplet in a Cassie state, $\cos\theta_3 = -1$. Hence,

$$cos\theta_{app} = -1 + sf_1 + sf_2 + (sf_1 + sf_2)cos\theta_{int}. \quad \text{(Eq. S15)}$$

Assuming an isotropic structure of a porous foam, the cross-sectional area ratio of fluid to the total can be approximated as $1 - sf_1 - sf_2$. For a porosity $\phi = 0.95$, we obtained $1 - sf_1 - sf_2 \sim \phi = 0.95$. Due to this very high cross-sectional area ratio of fluid, the difference in the apparent contact

angle on the porous foam could not be measured when the internal contact angle changed in hemiwicking state and Cassie state. In other words, superhydrophilic and superhydrophobic behaviors were observed over the regimes.

Considering the energy balance of the system for a droplet displacement on a heterogeneously coated porous foam in the Wenzel state,

$$dE = rf_p\left[rf_{local,1}sf_{1,local}(\gamma_{sl1} - \gamma_{sv1}) + rf_{local,2}sf_{2,local}(\gamma_{sl2} - \gamma_{sv2})\right]dx + \gamma_{lv}cos\theta_{app}dx \quad \text{(Eq. S16)}$$

where E is the free energy, dx is the droplet displacement, rf_p is the roughness factor defined as the ratio of total surface area of the porous foam to the projected surface area. Minimizing the free energy,

$$cos\theta_{app} = rf_p\left[rf_{local,1}sf_{1,local}\frac{\gamma_{sl1}-\gamma_{sv1}}{\gamma_{lv}} + rf_{local,2}sf_{2,local}\frac{\gamma_{sl2}-\gamma_{sv2}}{\gamma_{lv}}\right]. \quad \text{(Eq. S17)}$$

Substituting the Young equation $cos\theta = (\gamma_{sl} - \gamma_{sv})/\gamma_{lv}$ into Eq. S17,

$$cos\theta_{app} = rf_p\left[rf_{local,1}sf_{1,local}cos\theta_1 + rf_{local,2}sf_{2,local}cos\theta_2\right]$$

$$= rf_p cos\theta_{int}\ . \quad \text{(Eq. S18)}$$

In Figure 3E, the roughness factor of the sample without PTFE deposition (10 min nickel electrodeposition) $rf_p \approx 3.6$ obtained by the wicking test was used. An even sharper transition is expected for a higher roughness factor of a sample with PTFE deposition.

Note 4 – Roughness factor estimation for a porous foam by capillary rise test

The roughness factor is the input parameter for Wenzel equation (Eq. S18). We characterized the roughness factor of the nickel foam (thickness 1.6mm; width 15 mm; 10 min electrodeposition without PTFE particles) by the capillary rise test. When a tip of a porous foam was dipped into fluid, the fluid wicked and reached a certain height due to the capillarity. Based on an energy analysis, the wicking height h is given by[3]

$$h = \frac{S_v(\gamma_{sg}-\gamma_{sl})}{\rho_l g \phi}$$

$$= \frac{S_v \gamma_{lv} cos\theta}{\rho_l g \phi}. \qquad \text{(Eq. S19)}$$

Using a total wetting fluid, the specific area of a porous foam is obtained by the Eq. S19. The roughness factor rf_p was calculated by the following equation:

$$rf_p = S_v H \qquad \text{(Eq. S20)}$$

where H is the thickness of the porous foam. HFE7500 (density 1610 kg/m^3; surface tension 16.2 N/m) was used as a total wetting fluid in this experiment. We obtained 2.4 mm of the average wicking height which led to the specific area 2260 m^2/m^3 and a roughness factor 3.6.

Note 5 – Active bubble density analysis

We measured the active bubble population visible from the top view $n_{measured}$ (Figure S9). The active bubbles are defined as the bubbles which periodically grow and depart from the electrode. For the internal growth mode (PTFE coverage $\Theta_{PTFE} = 0$), the measured density of active bubbles $n_{measured} / A_{proj}$ was estimated as ≈ 1250 /cm^2 where A_{proj} is the projected area of the electrode. Assuming the same active bubble density for the internal structure, *i.e.*, $n_{total} / A_{total} = n_{measured} / A_{proj}$ where n_{total} is the total population of active bubbles both inside and on the surface of the porous electrode and A_{total} is the total area of the porous structure, the density of total active bubbles defined by the projected area is given by $n_{total} / A_{proj} = rf_p \, n_{total} / A_{total} = rf_p \, n_{measured} / A_{proj}$. The roughness factor rf_p ($= A_{total} / A_{proj}$) was determined by the wicking test (≈ 3.6). Thus, the active bubble density on the projected area for the internal growth mode was estimated as ≈ 4500 /cm^2. For the wicking mode (PTFE coverage $\Theta_{PTFE} = 0.16$), the measured active bubble density $n_{measured} / A_{proj}$ was estimated as ≈ 166 /cm^2. For the gas-filled mode, we observed a few large bubbles surrounded by many small bubbles (Figure S5 and Supplemental Video S3 and S4). However, the small bubbles rarely departed from the surface as observed in the video from the side view (Supplemental Video S3). For this reason, only the large bubbles, which periodically grew and departed from the electrode were regarded as the active bubbles. The active bubble density for the gas-filled mode ranged from 1 /cm^2 to 3 /cm^2.

Note 6 – Bubble departure diameter model

The bubble departure diameter is calculated by the Fritz equation, which is a widely used empirical correlation determined by equating the bubble holding force with the buoyant force on the bubble. As shown in Figure S8 the buoyancy F_b is the driving force of bubble departure, which is equal to $\rho_l g V$ where ρ_l, g, and V are the density of liquid solution, gravitational acceleration, and bubble volume, respectively. The forces act opposite to the buoyancy F_b are the gravity F_g and the vertical holding force F_h acting on the three-phase contact line due to the surface tension force F_s. The holding force F_h can be calculated by $F_h = 2\pi R sin^2\theta\gamma_{lv}$, where R, θ, and γ_{lv} are the bubble radius, contact angle and surface tension coefficient, respectively. Equating the buoyant force F_b with the gravity F_g and bubble holding force F_h with empirical corrections, the classic Fritz equation ($D_b = 0.0208\theta\{\gamma_{lv}/[g(\rho_l - \rho_v)]\}^{1/2}$) for the bubble departure diameter can be obtained.

Note 7 – Growth rate analysis

We measured and analyzed the bubble growth rate for the internal growth and departure, wicking, and gas-filled modes. Typically, bubble growth on relatively large active electrode surfaces is limited by diffusion.[4] For diffusive bubble growth, time evolution of bubble radius is described by,[1,5]

$$R = b\sqrt{t} \quad \text{(Eq. S21)}$$

$$b = \sqrt{R_d^2/t_r} \quad \text{(Eq. S22)}$$

where b is the growth coefficient, R_d is the bubble departure radius and t_r is the residence time.

For the internal bubble growth mode, the growth coefficient was determined in the following process. The volumetric flux of gas from gas evolving reaction is calculated by,[1]

$$\frac{\dot{V_g}}{A_{proj}} = \frac{n_{total}}{A_{proj}}\frac{V_d}{t_r} \quad \text{(Eq. S23)}$$

where V_d is the volume of bubble at departure. Meanwhile, the volumetric flux of gas can be also expressed as a function of the current density,[1]

$$\frac{\dot{V_g}}{A_{proj}} = \Phi_B f_g \frac{i_{nominal} R_g T}{v_e/v_B F p}\left(1 - \frac{p_s}{p}\right)^{-1} \quad \text{(Eq. S24)}$$

where Φ_B is the current efficiency (= 1), f_g is the gas efficiency, v_e is the charge number of the electrode reaction, v_B is the the stoichiometric number of the product, R_g is the universal gas constant, p_s is the vapor pressure of the solvent and p is the pressure. The gas efficiency is the ratio

of the number of the molecules to generate bubbles to the total number of the molecules produced by the reaction.

Combining Eq.S23 and Eq.S24, we obtain,

$$t_r = \frac{\frac{n_{total}}{A_{proj}} V_d \left(1 - \frac{p_s}{p}\right)}{\Phi_B f_g \frac{iRT}{v_e / v_B F p}} \quad \text{(Eq. S25)}$$

Assuming the typical range of the gas efficiency (f_g =0.2−0.6),[6,7] we estimated the growth coefficient and predicted bubble radius as shown in Figure 4D of the Main Text.

The time evolution of bubble radius for the internal growth and departure mode and gas-filled mode was directly obtained from the top view and side view images during the experiment. For the wicking mode (Θ_{PTFE} = 0.16), coalescence of bubbles was frequently observed and contributed to the bubble growth as shown in Figure 4E of the Main Text. We analyzed the bubble growth rates of multiple bubbles before coalescence occurred (Figure S7A). The growth coefficients ranged from 0.17 to 0.32 mm/s$^{0.5}$ which is in a comparable range to the internal growth and departure mode. For the gas-filled mode (Θ_{PTFE} = 0.55 and 0.76), the bubble growth coefficients ranged from 1.4 to 1.6 mm/s$^{0.5}$ which is much larger than the other two growth modes (Figure S7B). This result could be attributed to the gas transport through the internally connected pores. The results of bubble growth characterization for multiple bubbles are listed in Table S1.

Note 8 – Additional ohmic loss for the presence of bubbles

Ohmic voltage loss associated with the presence of the bubbles on the electrode is described by,[8]

$$\eta_{ohm,bub} = \frac{i_{nominal} L(1-K_m)}{\kappa K_m} \quad \text{(Eq. S26)}$$

where L is the bubble layer thickness, and K_m is the ratio of the effective conductivity to the electrolyte's intrinsic conductivity κ, which is the function of the gas void fraction f_b. Maxwell's equation is used to estimate K_m,[9]

$$K_m = \frac{1-f_b}{1+\frac{f_b}{2}}. \quad \text{(Eq. S27)}$$

The gas void fraction within the bubble layer is estimated by,

$$f_b = \frac{Total\ volume\ of\ bubbles\ on\ the\ electrode}{Volume\ of\ the\ bubble\ layer} = \frac{V_{b,ave} n_{proj}}{LA_{proj}} \quad \text{(Eq. S28)}$$

where $V_{b,ave}$ is the average bubble volume in the growth period. The average bubble radius in the diffusive growth period is estimated by

$$R_{ave} = \frac{\int_0^{t_r} R(t)dt}{t_r} = \frac{\int_0^{t_r} bt^{1/2}dt}{t_r} = \frac{2}{3} bt_r^{1/2} = \frac{2}{3} R_d \quad \text{(Eq. S29)}$$

where R is the bubble radius, R_d is the bubble departure radius.

Thus, the average bubble volume in the growth period is calculated as,

$$V_{b,ave} = \frac{\pi R_{ave}^3}{3} [4 - (2 + cos\theta)(1 - cos\theta)^2]. \quad \text{(Eq. S30)}$$

The bubble layer thickness, which is equal to the average height of the bubble H_{ave}, is thus given by,

$$L = H_{ave} = R_{ave}(1 + cos\theta). \quad \text{(Eq. S31)}$$

Based on these formulations, gas void fractions for the internal growth mode ($\Theta_{PTFE} = 0$), wicking mode ($\Theta_{PTFE} = 0.16$) and gas-filled mode ($\Theta_{PTFE} = 0.76$) were 0.065, 0.078 and 0.084, respectively. The bubble layer thickness for above three modes were 0.1 mm, 0.3 mm, and 1.8 mm, respectively. For the gas-filled mode, the gas void fraction due to the active large bubbles was 0.049 whereas the gas void fraction due to surrounding small bubbles was $f_b \approx 0.035$.

Note 9 – Bubble coverage analysis

The bubble coverage on an electrode is defined as,[1]

$$\Theta_{bubble} \equiv \frac{n_{total}}{A_{total} t_r} \int_0^{t_r} \pi (sin\theta R)^2 dt \quad \text{(Eq. S32)}$$

where t_r is the residence time of the bubble, R is the bubble radius. Assuming the diffusive growth of bubbles,[1]

$$\Theta_{bubble} = \frac{n_{total}}{2A_{total}} \pi (sin\theta R_d)^2 \quad \text{(Eq. S33)}$$

where R_d is the bubble departure radius.

For the internal bubble growth mode, the bubble coverage was 0.001, leading to a bubble overpotential of 0.1 mV. Thus, owing to the small base area of bubble, the bubble overpotential was negligible in this mode. For the wicking mode, the projected bubble coverage from the image was 0.35 (Figure S9). Considering the contact angle of 12°, the corrected bubble coverage is 0.015. However, the actual bubble coverage could be higher than this value since gas uptake inside the porous structure was not accounted into our estimation. For the gas-filled mode, the projected bubble coverage from the images were 0.4 and 0.47 for PTFE coverage of 0.55 and 0.76, respectively (Figure S9).

Supplemental References

1. Vogt, H., and Balzer, R.J. (2005). The bubble coverage of gas-evolving electrodes in stagnant electrolytes. Electrochim. Acta *50*, 2073–2079.

2. Vogt, H. (2012). The actual current density of gas-evolving electrodes - Notes on the bubble coverage. Electrochim. Acta *78*, 183–187.

3. de Gennes, P.-G., Brochard-Wyart, F., and Quéré, D. (2004). Capillarity and wetting phenomena.

4. Van Der Linde, P., Moreno Soto, Á., Peñas-López, P., Rodríguez-Rodríguez, J., Lohse, D., Gardeniers, H., Van Der Meer, D., and Fernández Rivas, D. (2017). Electrolysis-Driven and Pressure-Controlled Diffusive Growth of Successive Bubbles on Microstructured Surfaces. Langmuir *33*, 12873–12886.

5. Van Der Linde, P., Moreno Soto, Á., Peñas-López, P., Rodríguez-Rodríguez, J., Lohse, D., Gardeniers, H., Van Der Meer, D., and Fernández Rivas, D. (2017). Electrolysis-Driven and Pressure-Controlled Diffusive Growth of Successive Bubbles on Microstructured Surfaces. Langmuir *33*, 12873–12886.

6. Vogt, H. (1984). The rate of gas evolution of electrodes-I. An estimate of the efficiency of gas evolution from the supersaturation of electrolyte adjacent to a gas-evolving electrode. Electrochim. Acta *29*, 167–173.

7. Chin Kwie Joe, J.M., Janssen, L.J.J., van Strelen, S.J.D., Verbunt, J.H.G., and Sluyter, W.M. (1988). Bubble parameters and efficiency of gas bubble evolution for a chlorine-, a

hydrogen- and an oxygen-evolving wire electrode. Electrochim. Acta *33*, 769–779.

8. Leistra, J.A., Sides, P.J., Soc, J.E., Leistra, J.A., and Sides, P.J. (1987). Voltage Components at Gas Evolving Electrodes. J. Electrochem. Soc. *134*, 2442–2446.

9. Zhao, X., Ren, H., and Luo, L. (2019). Gas Bubbles in Electrochemical Gas Evolution Reactions. Langmuir *35*, 5392–5408.